Journal of Materials Chemistry C

ROYAL SOCIETY OF CHEMISTRY

PAPER

View Article Online
View Journal | View Issue

Check for updates

Cite this: J. Mater. Chem. C, 2024, 12, 14013

Environmentally stable Mn-doped $CsPbX_3$@$CsPb_2X_5$ core–shell materials with efficient energy transfer†

Chen Zhang,[a] Luxia Xu,[b] Minqiang Wang,*[a] Zheyuan Da,[a] Jindou Shi,[a] Junnan Wang,[a] Qing Yao,[a] Jinshou Tian,[b] Nikolai V. Gaponenko[c] and Youlong Xu[a]

Received 22nd March 2024,
Accepted 26th July 2024

DOI: 10.1039/d4tc01135j

rsc.li/materials-c

Mn(II)-doped cesium lead halide perovskite ($CsPbX_3$ (X = Cl, Br, I)) quantum dots (QDs) have attracted a lot of attention from researchers attributed to their bright orange light emission. However, defects such as inefficient energy transfer and instability have hindered the commercial application of the material. Here, we propose a convenient core–shell coating strategy to epitaxially grow a $CsPb_2X_5$ shell on Mn-doped $CsPbX_3$ surfaces by controlling the reaction time and precursor ratio. Meanwhile, density-functional theory (DFT) calculations indicate that a typical type-I heterojunction is formed between the $CsPb(Cl/Br)_3$ cores and the $CsPb_2(Cl/Br)_5$ shell, which improves the energy transfer efficiency from an exciton to Mn^{2+}. The obtained Mn-doped $CsPb(Cl/Br)_3$@$CsPb_2(Cl/Br)_5$ core–shell materials exhibit enhanced optical properties and excellent water/thermal stability. Subsequently, the white light-emitting diode prepared from the composites shows a high luminescence efficiency of 127.21 lm W^{-1}, and the PL intensity is still maintained above 95% after 24 h of continuous operation.

Published on 27 July 2024. Downloaded by Xian Jiaotong University on 10/11/2024 2:45:41 AM.

Introduction

Cesium lead halide ($CsPbX_3$ (X = Cl, Br, I)) perovskite quantum dots (QDs) have become one of the most promising materials in the field of optoelectronics due to high absorption coefficients and quantum yields close to 100%.[1–5] However, their inherent monochromatic emission and sensitivity to the surroundings limit their further commercial application.[6] Doping new luminescent centers has proved to be an effective means to resolve monochromatic light emission.[7–9] Especially for Mn^{2+} ions, the large energy difference between the exciton energy level and the Mn^{2+} excited state energy level significantly inhibits the reverse energy transfer, making the synthesis and luminescence properties of Mn-doped perovskite quantum dots of wide interest to researchers.[10–13] But, due to differences in ionic radii and surface charges, these additional luminescent centers have the potential to cause the host to lose its intrinsic crystal structure and emission.[14–16] Therefore, a convenient improvement strategy is necessary to enhance the energy transfer efficiency from excitons to Mn^{2+} ions while maintaining the crystal structure stability of the perovskite host.

Currently, in most reports of Mn-doped $CsPbX_3$ QDs broad emission peaks at 600 nm have been observed, and Mn^{2+} emission usually coexists with exciton emission.[17,18] This inevitably leads to exciton energy transfer competing with the radiative/non-radiative transitions of the exciton, resulting in inefficient Mn^{2+} emission.[19,20] According to previous reports, if quantum confinement is imposed on the exciton of the perovskite host, this exchange coupling effect can lead to modified spatial distribution of the dopant, thus improving the exciton to Mn^{2+} energy transfer efficiency.[21,22] Therefore, the core–shell structure provides a new idea to solve the above problem, because the heterogeneous shell can effectively limit the diffusion length of excitons either at spatial or energy levels.[23,24] Meanwhile, this approach not only significantly improves stability but also allows the formation of high-quality heterojunctions, providing a platform for exploring novel photophysical properties.[25,26]

Here, we propose an improved hot-injection method to epitaxially grow $CsPb_2X_5$ shells on the surface of Mn-doped $CsPbX_3$ QDs by using controlled precursor ratios and extended

[a] Electronic Materials Research Laboratory, Key Laboratory of the Ministry of Education International Center for Dielectric Research&Shannxi Engineering Research Center of Advanced Energy Materials and Devices, Xi'an Jiaotong University, 710049 Xi'an, China. E-mail: mqwang@xjtu.edu.cn
[b] Xi'an Institute of Optics and Precision Mechanics, CAS, Add: NO. 17 Xinxi Road, New Industrial Park, Xi'an Hi-Tech Industrial Development Zone, 710119 Xi'an, Shaanxi, China
[c] Belarusian State University of Informatics and Radioelectronics, P. Browki 6, 220013 Minsk, Belarus

† Electronic supplementary information (ESI) available. See DOI: https://doi.org/10.1039/d4tc01135j

Published on 27 July 2024. Downloaded by Xian Jiaotong University on 10/11/2024 2:45:41 AM.

reaction times. As the Mn doping concentration increases, the light emission of the $CsPbX_3$@$CsPb_2X_5$ core–shell materials gradually changes from blue to pink. Moreover, compared to pure $CsPbX_3$ QDs, the composite exhibits stronger Mn^{2+} emission at low doping concentrations. According to density-functional theory (DFT) calculations, this phenomenon is attributed to the type-I heterojunction constituted between $CsPbX_3$ and $CsPb_2X_5$, which allows more carriers to accumulate in the $CsPbX_3$ energy band, thus alleviating the competition for energy transfer from excitons to Mn^{2+}. Benefiting from the stable crystal structure of $CsPb_2X_5$, the water/thermal stability of $CsPbX_3$ QDs is significantly improved. Finally, the white LEDs prepared from these composites exhibit a surprisingly high luminous efficacy of 127.41 lm W^{-1} and sustained operating stability at high temperature (>95 °C).

Results and discussion

Morphology and crystal structure of Mn-doped $CsPb(Cl/Br)_3$@$CsPb_2(Cl/Br)_5$

Mn-doped $CsPb(Cl/Br)_3$@$CsPb_2(Cl/Br)_5$ core–shell materials could be obtained directly by using a hot-injection method without an additional post-treatment process. Briefly, a total of 0.3 mmol of $MnCl_2$ and $PbBr_2$ was dissolved in 1-octadecene (ODE). Subsequently, 0.15 mmol of Cs-OA (Cs : Pb = 1 : 2) was injected at high temperature. After 1 h of reaction, Mn-doped $CsPb(Cl/Br)_3$@$CsPb_2(Cl/Br)_5$ core–shell materials could be obtained (denoted as MCC composites).

First, the morphology of the products was observed by scanning electron microscopy (SEM) and transmission electron microscopy (TEM). The results showed that the MCC composites were uniform octagonal microplates with an average size of about 5.27 μm (Fig. 1a and b). Moreover, the grains had a smooth surface, preliminarily indicating that $CsPb(Cl/Br)_3$ QDs had been encapsulated by $CsPb_2(Cl/Br)_5$ (Fig. 1a, inset). Furthermore, in order to demonstrate that the composites had a core–shell structure, we observed the interior of the octagonal microplates by TEM. The results showed that a large number of $CsPb(Cl/Br)_3$ QDs with a size of about 10–15 nm were embedded inside the grains (Fig. 1c). Moreover, benefiting from the protection of the $CsPb_2(Cl/Br)_5$ shell, the QDs still maintained their original cubic morphology without agglomeration or decomposition caused by the prolonged high-temperature reaction. Subsequently, energy dispersive spectroscopy (EDS) showed that Cs, Pb, Mn, Br, and Cl were uniformly distributed in the whole grains of the MCC composites, proving the successful doping of Mn^{2+} ions (Fig. 1d). It was worth noting that since no aggregation of Mn^{2+} was observed, Mn^{2+} was not only present in the $CsPb(Cl/Br)_3$ QDs, but the $CsPb_2(Cl/Br)_5$ shell was also doped with Mn^{2+}.

Subsequently, the crystal structures of the MCC composites were observed by high-resolution TEM (HRTEM). As shown in Fig. 2a, the composites had two different lattice fringes, where 0.74 nm belonged to the (002) plane of the tetragonal (β) $CsPb_2(Cl/Br)_5$; and 0.57 nm belonged to the (100) plane of the cubic (α) $CsPb(Cl/Br)_3$. This result was slightly smaller than the standard 0.583 nm (α-$CsPbBr_3$ (100) plane) and 0.758 nm (β-$CsPb_2Br_5$ (002) plane). This phenomenon was attributed to the lattice shrinkage caused by the substitution of the larger ionic radius Pb^{2+} and Br^- with the smaller ionic radius Mn^{2+} and Cl^-.[27,28] The corresponding selected-area electron

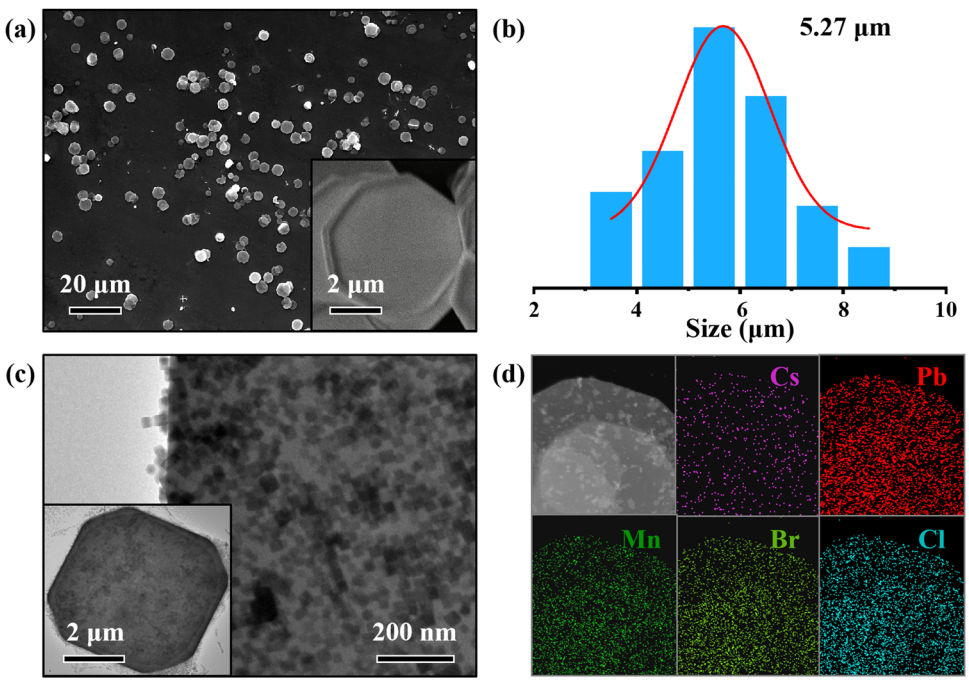

Fig. 1 (a) SEM images of overall morphology and individual grains (inset) of the MCC composites. (b) The size distribution of the MCC composites. (c) TEM images of the interior and individual grains (inset) of the MCC composites. (d) Elemental mapping of the MCC composites.

 This journal is © The Royal Society of Chemistry 2024

Published on 27 July 2024. Downloaded by Xian Jiaotong University on 10/11/2024 2:45:41 AM.

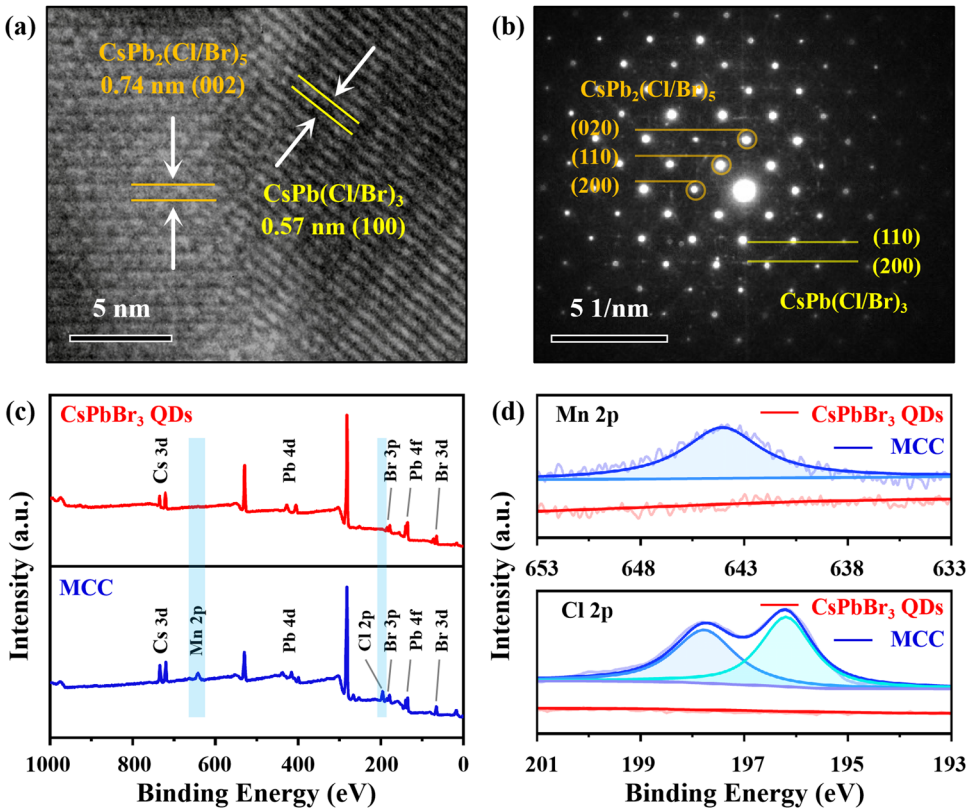

Fig. 2 (a) HRTEM image and (b) SAED pattern of the MCC composites. (c) XPS spectra of the MCC composites and $CsPbBr_3$ QDs. (d) High-resolution XPS spectra of Mn 2p and Cl 2p.

diffraction (SAED) image consisted of clear single-crystal diffraction spots and polycrystalline rings (Fig. 2b), demonstrating that the overall structure of the MCC composites was a $CsPb_2(Cl/Br)_5$ single-crystal shell encasing a large number of $CsPb(Cl/Br)_3$ QDs, and that both possessed excellent crystallinity. Furthermore, in order to determine the chemical components of the composites, we performed X-ray photoelectron spectroscopy (XPS) measurements (Fig. 2c). Compared to the $CsPbBr_3$ QDs, the MCC composites showed distinct Mn and Cl signals. Among them, the peak at 644.0 eV was assigned to Mn 2p; the two peaks at 197.7 eV and 196.2 eV were assigned to Cl 2p (Fig. 2d). Meanwhile, the Pb signal was significantly reduced after Mn^{2+} doping, proving that Mn^{2+} successfully replaced Pb^{2+} in the lattice. In addition, the signals of Cs 3d, Pb 4f and Br 3d of the MCC composites were all slightly shifted toward a higher binding energy (Δ eV $\approx$ 0.5–0.7 eV), suggesting that after the passivation of the $CsPb_2X_5$ shell, the electron density of $CsPbX_3$ was reduced, attributed to the strong sharing of reactive atoms (mainly Pb) between 0D $CsPbBr_3$ and 2D $CsPb_2Br_5$ (Fig. S1a–c, ESI†).[29,30] In summary, the SEM and TEM results demonstrated that the core–shell structured MCC composites could be conveniently obtained by simply controlling the reaction time and precursor ratio.

Optical properties of Mn-doped $CsPb(Cl/Br)_3$@$CsPb_2(Cl/Br)_5$

Furthermore, we investigated the effect of Mn^{2+} doping concentration on the optical properties of the samples, in order to find the optimal Mn doping ratio. At first, ICP-OES was used to accurately quantify the concentration of Mn^{2+} in the samples. An error between the initial Mn/Pb feed ratio and the actual doping ratio could be found, and the highest Mn^{2+} doping ratio was 51% (Table S1, ESI†). Moreover, the MCC composites had two distinct emission centers corresponding to exciton emission (400–500 nm) and d–d transition of Mn^{2+} ($\approx$600 nm) (Fig. 3a). The corresponding PL excitation (PLE) spectra showed that the sample had a strong absorption at 300–450 nm, corresponding to the exciton absorption peak (Fig. S2, ESI†) whereas, there was almost no absorption at 450–550 nm, indicating that the Mn^{2+} emission was mainly dominated by the energy transfer from excitons to Mn^{2+} ions. As the doping concentration increased (Mn/Pb = 0.5–2.0), the exciton emission was blue-shifted and the PL intensity decreased, while Mn^{2+} emission was enhanced and gradually dominated. The emission of the samples also gradually changed from blue to pink light (Fig. 3a, inset). However, as the concentration of Mn^{2+} increased further (Mn/Pb = 2.5), due to the gradual decrease of the distance between the emission centers, the cross-relaxation rate increased and the PL intensity showed a decreasing trend.[31,32] In this process, the exciton emission blue-shift was attributed to the selected Mn-source, $MnCl_2$, where the increased Mn^{2+} concentration led to the Cl-rich host. Therefore, the exciton emission peak changed from 488 nm to 427 nm, while the raised intensity of Mn^{2+} emission probably implied a more efficient energy transfer process. To demonstrate this, we prepared $CsPbX_3$ QDs with the same

Published on 27 July 2024. Downloaded by Xian Jiaotong University on 10/11/2024 2:45:41 AM.

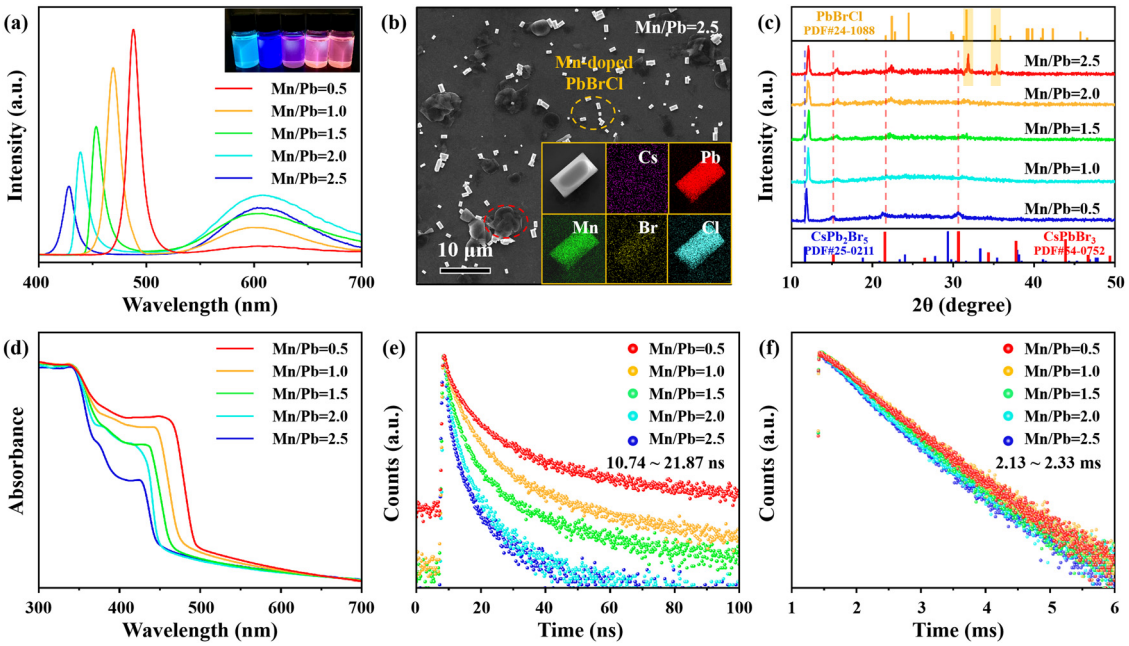

Fig. 3 (a) PL spectra of MCC composites with different Mn^{2+} doping amounts (λ = 365 nm). (b) SEM images and elemental mapping of MCC composites (Mn/Pb = 2.5). (c) XRD patterns and (d) UV-Vis absorption spectra of MCC composites with different Mn^{2+} doping amounts. Time-resolved fluorescence spectra of (e) excitons and (f) Mn^{2+} ions in MCC composites with different Mn^{2+} doping amounts.

doping concentration to reveal the optical enhancement effect of the $CsPb_2X_5$ shell. Fig. S3 (ESI†) exhibited an overall morphology of Mn-doped $CsPbX_3$ (Mn/Pb = 2.0) QDs. The Mn-doped $CsPb(Cl/Br)_3$ QDs without $CsPb_2(Cl/Br)_5$ coating were typically cubic grains (Fig. S4b, ESI†), and some QDs had decomposed or agglomerated due to the high concentration of Mn doping (Fig. S3a, ESI†). This was consistent with the TEM observations (Fig. S3b, ESI†). Subsequently, PL spectra showed that at low doping concentrations (Mn/Pb = 0.5–1.5), the Mn^{2+} emission was masked by strong exciton emission (Fig. S4a, ESI†). Only when the Mn/Pb increased above 2.0, a slight Mn^{2+} emission was observed. In contrast, when Mn/Pb = 1.0, a visible Mn^{2+} emission was observed in the MCC composites; when Mn/Pb = 1.5, the emission of the sample transformed to pink light, proving that the electron decay route had been dominated by the energy transfer process. Therefore, MCC composites had higher energy transfer efficiency.

Furthermore, we revealed the effect of high concentration of the dopant on the sample morphology by SEM. The results showed that at Mn/Pb = 2.5, the MCC composites were fragmented due to excessive Mn^{2+} doping (shown as red circles in Fig. 3b) and unknown rectangular grains were formed (shown as orange circles in Fig. 3b). The elemental mapping indicated that these rectangular grains were enriched with Pb, Mn, Cl, and Br, while Cs hardly contributed (Fig. 3b inset). Meanwhile, the corresponding XRD patterns showed that at Mn/Pb = 2.5, the MCC composites were composed of $CsPb_2X_5$ and PbBrCl (Fig. 3c). Based on these two results, we concluded that the rectangular grain was Mn-doped PbClBr. The formation of PbBrCl impurity might be one of the reasons that the optical properties of MCC composites were deteriorated. This was attributed to the fact that the exciton energy transfer to Mn d-states depended on the host band gap and relative positions of Mn $^4T_1$ and $^6A_1$ states. In the $CsPbX_3$ host, Mn^{2+} acquired strain-free Pb sites with fixed coordination of six, resulting in a strong Mn d–d emission. However, in the PbX_2 host, Mn^{2+} could only occupy the Pb sites with a coordination of two, which was in an under-coordinated state. Therefore, Mn emission was quenched at Mn/Pb = 2.5.[33] Subsequently, the ultraviolet-visible (UV-Vis) absorption spectra of the composites exhibited the band-edge absorption (400–500 nm) of $CsPbX_3$ QDs, further demonstrating that the $CsPb_2X_5$ shell would not affect the intrinsic optical properties of the internal QDs (Fig. 3d). In addition, in order to visually demonstrate the optical enhancement effect of $CsPb_2X_5$ shell, we compared the PL decay lifetimes of MCC composites and $CsPbX_3$ QDs. The results showed that the average lifetimes of the excitons in MCC composites were 10.74–21.87 ns (Fig. 3e), while the QDs were only 6.83–13.86 ns (Fig. S4c, ESI†), which were improved by 55–82% (Table S2, ESI†); the average lifetimes of Mn^{2+} were 2.13–2.33 ms (Fig. 3f), which were improved by 70–80% (QDs: 1.26–1.36 ms (Fig. S4d, ESI†)). This phenomenon demonstrated that the $CsPb_2X_5$ shell effectively passivated the surface defects of QDs and improved the radiative recombination efficiency.[34] The PLQY exhibited similar results. The PLQY of MCC composites were 68–78%, while the Mn-doped $CsPb(Cl/Br)_3$ QDs were only 31–57% (Fig. S5, ESI†).

Finally, we calculated the energy transfer efficiency from excitons to Mn^{2+} ions in MCC composites as reported by Zhong *et al.*[20] At first, we prepared $CsPb(Cl/Br)_3$@$CsPb_2(Cl/Br)_5$ composites without Mn doping by using an anion-exchange method, and made the PL position of the composites

 This journal is © The Royal Society of Chemistry 2024

Published on 27 July 2024. Downloaded by Xian Jiaotong University on 10/11/2024 2:45:41 AM.

consistent with the MCC composites. Ideally, the only difference between the two samples would be that $CsPb(Cl/Br)_3$@$CsPb_2(Cl/Br)_5$ was undoped with Mn^{2+}, while the MCC composites was doped with Mn^{2+}. Subsequently, PL decay showed that the average lifetime of excitons in $CsPb(Cl/Br)_3$@$CsPb_2(Cl/Br)_5$ was 16.64–29.05 ns (Fig. S6, ESI†), while the average lifetime of excitons in MCC composites was 10.74–21.87 ns. The significant decrease in exciton lifetime proved the existence of energy transfer from excitons to Mn^{2+}. Therefore, the energy transfer efficiency (η_{ET}) from excitons to Mn^{2+} could be calculated by the following equation:

$$\eta_{ET} = 1 - \frac{\tau_1}{\tau_0}$$

where τ_0 and τ_1 are the lifetimes of exciton emission without or with Mn^{2+}. Specifically, τ_0 represents the exciton emission lifetime of $CsPb(Cl/Br)_3$@$CsPb_2(Cl/Br)_5$ and τ_1 represents the exciton emission lifetime of the MCC composites. Calculations showed that the MCC composites with Mn/Pb = 2.0 (corresponding to the PL position of 439 nm) had the best energy transfer efficiency (42.0%) (Table S3, ESI†).

Energy band structure and water/thermal stability of Mn-doped $CsPb(Cl/Br)_3$@$CsPb_2(Cl/Br)_5$

The energy band structure of the MCC composites was also one of the key factors affecting its optical properties. Therefore, we calculated the electronic structures of Mn-doped $CsPb(Cl/Br)_3$ cores and Mn-doped $CsPb_2(Cl/Br)_5$ shell (Mn/Pb = 2.0) based on density-functional theory (DFT). Among them, the Mn-doped $CsPb(Cl/Br)_3$ cores had the band gap of 1.44 eV (Fig. 4a), while the $CsPb(Cl/Br)_3$ host was 2.83 eV (Fig. S7a, ESI†), which evidenced that Mn^{2+} acted as an additional channel for receiving and accumulating photogenerated carriers, introducing additional energy levels in the forbidden band.[35–37] The corresponding projected density of states (PDOS) showed that the conduction band was mainly contributed by Mn (d); the valence band was dominated by Cl (3p) and Br (3p) (Fig. 4b). Thus, the energy band structure of Mn-doped $CsPb(Cl/Br)_3$ cores is shown in Fig. 4c. When the sample was excited, the radiative transitions of photogenerated carriers were mainly in the following two routes: (1) recombination in the energy band of $CsPb(Cl/Br)_3$ to produce the corresponding exciton emission; (2) undergoing the energy transfer process to produce the $^4T_1 \rightarrow {}^6A_1$

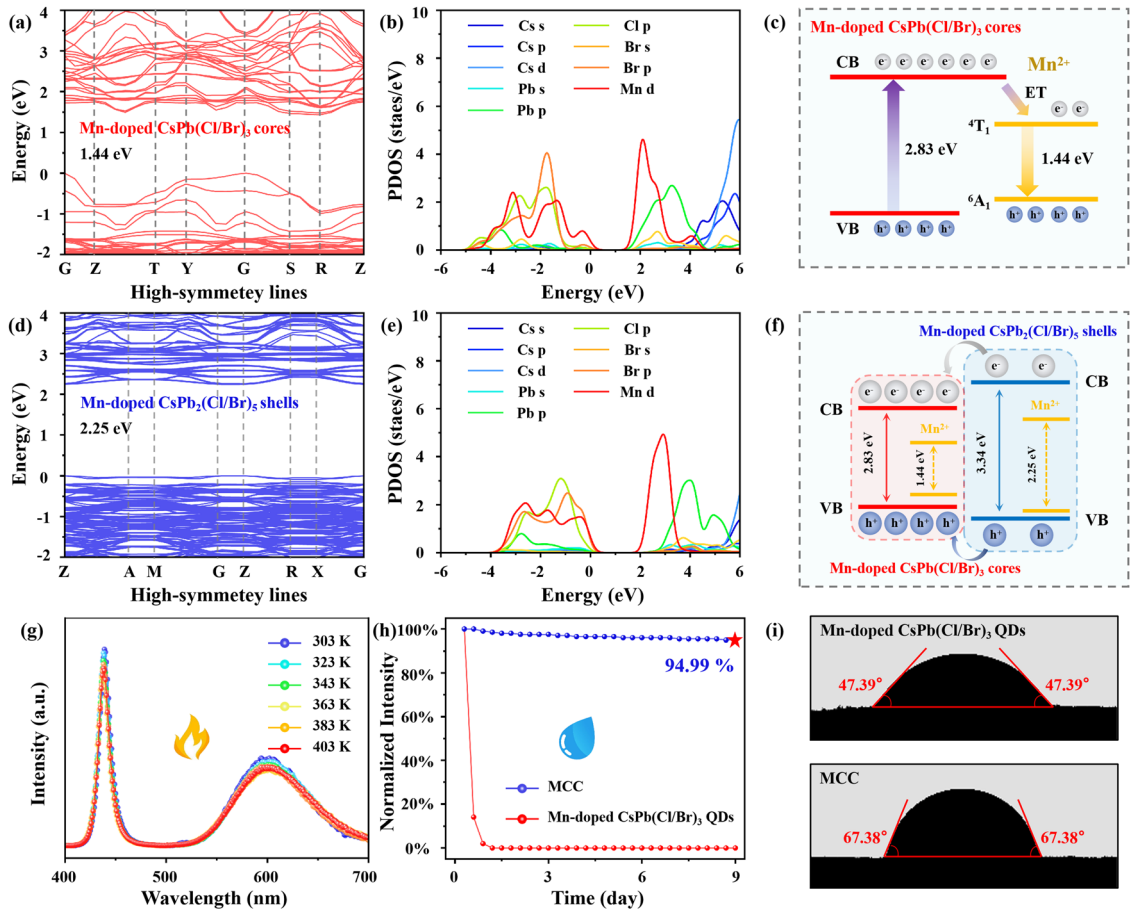

Fig. 4 (a) Electronic structure, (b) projected density of states and (c) energy band structure of Mn^{2+} doped $CsPb(Cl/Br)_3$ cores (Mn/Pb = 2.0). (d) Electronic structure and (e) projected density of states of Mn^{2+} doped $CsPb_2(Cl/Br)_5$ shells (Mn/Pb = 2.0). (f) Energy band structure of MCC composites (Mn/Pb = 2.0). (g) Temperature-dependent PL spectra of MCC composites (Mn/Pb = 2.0) at 303–403 K. Comparison of (h) water stability and (i) water contact angle between MCC composites (Mn/Pb = 2.0) and Mn-doped $CsPb(Cl/Br)_3$ QDs.

Published on 27 July 2024. Downloaded by Xian Jiaotong University on 10/11/2024 2:45:41 AM.

emission (≈600 nm) in the energy band of Mn^{2+}.[18,38] The Mn-doped $CsPb_2(Cl/Br)_5$ shell (Mn/Pb = 2.0) was similar to the above results, with a band gap of 2.25 eV (Fig. 4d), which was much smaller than the $CsPb_2(Cl/Br)_5$ host (3.34 eV, Fig. S7b, ESI†). And, the conduction and valence bands were dominated by Mn (d) and Cl/Br (3p) (Fig. 4e). It is worth noting that, in general, the Mn d-states were insensitive to particle size or composition. In the $CsPbX_3$ host, Mn^{2+} replaced Pb^{2+} in PbX_6 to obtain strain-free Pb sites with a fixed coordination of six. Thus, whether in $CsPbCl_3$, $CsPbBr_3$ or $CsPbI_3$, the energy difference between the $^6A_1$ and $^4T_1$ orbitals from Mn would not be affected by the surroundings. However, in the $CsPb_2X_5$ host, Mn replaced Pb^{2+} in PbX_8, obtaining Pb sites with a fixed coordination to eight, leading to the change in the energy difference between the $^6A_1$ and $^4T_1$ orbitals (1.44 eV to 2.25 eV). But interestingly, from the overall energy band structure of the MCC composites, a typical type-I heterojunction was formed between $CsPb(Cl/Br)_3$ and $CsPb_2(Cl/Br)_5$ (Fig. 4f), which implied that the $CsPb(Cl/Br)_3$ cores had more electron–hole pairs, which could effectively alleviate the competition for energy transfer and improve the energy transfer efficiency from exciton to Mn^{2+}.[17,39,40] Therefore, MCC composites possessed stronger Mn^{2+} emission than QDs at the same Mn^{2+} doping concentration.

Finally, we evaluated the water/thermal stability of the MCC composites (Mn/Pb = 2.0) to confirm that the materials had the basis for commercial application. First, the thermal stability results showed that for pure $CsPbX_3$ QDs, the PL intensity decreased dramatically with increasing temperature (303–403 K) and the exciton emission were significantly blue-shifted (Fig. S8, ESI†). However, the MCC composites showed excellent thermal stability. Undergoing the same warming process, the PL intensity of the samples only decayed by ~9% and the PL position was not shifted (Fig. 4g). Furthermore, water stability had similar results. For the $CsPbX_3$ QDs, the samples were already quenched after a few hours of immersion, due to the dissolution of the crystal structure by water (Fig. 4h). In contrast, the MCC composites retained 94.99% of their PL intensity after 9 days of immersion, decaying by only ~5%. This was attributed to the fact that the MCC films had a higher water contact angle than the QDs films, and water could not easily penetrate inside the materials (Fig. 4i). Meanwhile, the high decomposition enthalpy of $CsPb_2X_5$ in water gave the MCC composites a surprising water stability.[41,42]

Optical properties and stability of WLEDs

White light-emitting diodes (WLEDs), one of the most prominent applications of $CsPbX_3$ QDs, where optical properties and stability determined the material's development prospects.[37,43] We prepared a quasi-perovskite white LED (denoted as M-WLED) by encapsulating the MCC composites (Mn/Pb = 2.0, red and blue emission source) and $CsPbBr_3$@$CsPb_2Br_5$ (green emission source) in polystyrene to make polymer films, and then, integrating them onto a 365 nm UV chip. Similarly, we used $CsPbX_3$ QDs without $CsPb_2X_5$ assembled into white LEDs as a comparison (denoted as C-WLED).

First, the PL spectra showed that the device could clearly distinguish the emission of blue, green, and orange phosphors (Fig. 5a), with the corresponding CIE coordinates of (0.318, 0.326) (Fig. 5b). Furthermore, the M-WLED had the maximum luminous efficiency of 127.21 lm W^{-1} (19 mA), and the color rendering index (CRI) was stable above 87 and up to 93 (Fig. 5c). But the maximum luminous efficiency of the C-LED was only

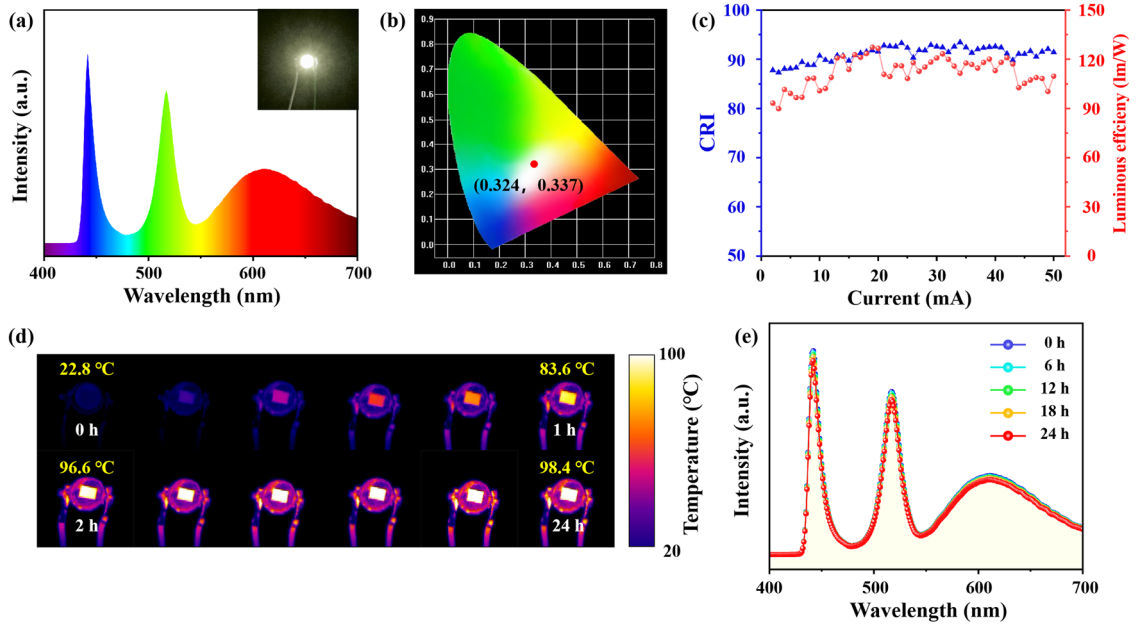

Fig. 5 (a) PL spectrum of M-WLED at 20 mA drive current. The inset shows the photo of the device. (b) CIE coordinates of the M-WLED at 20 mA drive current. (c) Luminous efficiency and color rendering index of M-WLED at 2–50 mA driving current. (d) Surface temperature and (e) PL spectra of M-WLED continuously operated for 24 h at 20 mA driving current.

 This journal is © The Royal Society of Chemistry 2024

Published on 27 July 2024. Downloaded by Xian Jiaotong University on 10/11/2024 2:45:41 AM.

87.39 lm W^{-1}, and the CRI gradually decreased with increase of the drive current, and finally was only 57 (Fig. S9, ESI†). Finally, since the optoelectronic devices inevitably generated high temperatures during continuous operation, this could lead to thermal decomposition of the $CsPbX_3$ QDs. Therefore, we recorded the surface temperature and PL spectra of M-WLED at different operating times to demonstrate that the MCC composites had long-term operational stability. The results indicated that the surface temperature of the M-WLED increased to over 80 °C after 1 h of operation and stabilized at 95–100 °C in the following 2–24 h (Fig. 5d). Obviously, such high temperature environments would significantly deteriorate the optical properties of QDs. However, the PL intensity of M-WLED remained above 95% after 24 h of continuous operation and the PL position was not shifted (Fig. 5e). Therefore, the strategy of using $CsPb_2X_5$ single-crystal shell as a protective layer to passivate Mn-doped $CsPbX_3$ QDs would be able to greatly expand the applications of pervoskite materials in the field of optoelectronics.

Conclusions

In summary, Mn-doped $CsPb(Cl/Br)_3$@$CsPb_2(Cl/Br)_5$ core–shell materials could be conveniently obtained by controlling the reaction time and the precursor ratio. The composites had a uniform octagonal morphology, and the $CsPb_2(Cl/Br)_5$ shell could effectively protect the $CsPb(Cl/Br)_3$ cores to withstand prolonged high-temperature reactions without agglomeration or decomposition. Subsequently, DFT calculations showed that a typically type-I heterojunction was constituted between the two, which led to the accumulation of more electron–hole pairs on the $CsPb(Cl/Br)_3$ cores, alleviating the competition for energy transfer and improving the energy transfer efficiency from excitons to Mn^{2+}. Benefiting from the stabilized crystal structure of the $CsPb_2X_5$ shell, the fluorescence lifetime and stability of the composites were significantly improved. The quasi-white LEDs prepared from the composites exhibited a high luminous efficiency of 127.21 lm W^{-1} and a high color rendering index of 93, and the PL intensity was basically unchanged after 24 h of operation at high temperature above 95 °C. This strategy provided a new idea for further applications of Mn-doped perovskite quantum dots.

Data availability

The data supporting this article have been included as part of the ESI.†

Conflicts of interest

There are no conflicts of interest to declare.

Acknowledgements

This work was supported by the National Key R&D Program of China (2022YFE0122500 and 2019YFB1503200), the National Natural Science Foundation of China (NSFC, 52161145103 and 61774124), the 111 Program (No. B14040), and the Shaanxi Provincial Key Research and Development Program (No. 2021GXLH-Z-084). The authors thank Ms Dan He at Instrument Anaysis Center of Xi'an Jiaotong University for her help with the time-resolved PL analysis.

References

1 L. Protesescu, S. Yakunin, M. I. Bodnarchuk, F. Krieg, R. Caputo, C. H. Hendon, R. X. Yang, A. Walsh and M. V. Kovalenko, *Nano Lett.*, 2015, **15**, 3692–3696.
2 K. Lin, J. Xing, L. N. Quan, F. P. G. de Arquer, X. Gong, J. Lu, L. Xie, W. Zhao, D. Zhang, C. Yan, W. Li, X. Liu, Y. Lu, J. Kirman, E. H. Sargent, Q. Xiong and Z. Wei, *Nature*, 2018, **562**, 245–248.
3 S. Chen, J. Lin, J. Huang, T. Pang, Q. Ye, Y. Zheng, X. Li, Y. Yu, B. Zhuang and D. Chen, *Adv. Funct. Mater.*, 2023, **34**, 2309293.
4 J. Lin, S. Chen, W. Ye, Y. Zeng, H. Xiao, T. Pang, Y. Zheng, B. Zhuang, F. Huang and D. Chen, *Adv. Funct. Mater.*, 2024, **34**, 2314795.
5 S. Chen, J. Lin, S. Zheng, Y. Zheng and D. Chen, *Adv. Funct. Mater.*, 2023, **33**, 2213442.
6 E. Jang and H. Jang, *Chem. Rev.*, 2023, **123**, 4663–4692.
7 L. Ruan and Y. Zhang, *Nat. Commun.*, 2021, **12**, 219.
8 G. Pan, X. Bai, D. Yang, X. Chen, P. Jing, S. Qu, L. Zhang, D. Zhou, J. Zhu, W. Xu, B. Dong and H. Song, *Nano Lett.*, 2017, **17**, 8005–8011.
9 G. Pan, X. Bai, W. Xu, X. Chen, D. Zhou, J. Zhu, H. Shao, Y. Zhai, B. Dong, L. Xu and H. Song, *ACS Appl. Mater. Interfaces*, 2018, **10**, 39040–39048.
10 H. S. Jung, H. Choe, J. Park, Y. Kim, S. J. Oh, S. J. Ryu, H. K. Na, S. J. Lee, K. C. Neuman, J. Cho and J. H. Shim, *ACS Appl. Mater. Interfaces*, 2023, **15**, 51593–51605.
11 W. J. Mir, M. Jagadeeswararao, S. Das and A. Nag, *ACS Energy Lett.*, 2017, **2**, 537–543.
12 L. Wu, Y. Wang, M. Kurashvili, A. Dey, M. Cao, M. Doblinger, Q. Zhang, J. Feldmann, H. Huang and T. Debnath, *Angew. Chem., Int. Ed.*, 2022, **61**, e202115852.
13 K. Zhang, J. Zhao, Q. Hu, S. Yang, X. Zhu, Y. Zhang, R. Huang, Y. Ma, Z. Wang, Z. Ouyang, J. Han, Y. Han, J. Tang, W. Tong, L. Zhang and T. Zhai, *Adv. Mater.*, 2021, **33**, e2008225.
14 A. K. Guria, S. K. Dutta, S. D. Adhikari and N. Pradhan, *ACS Energy Lett.*, 2017, **2**, 1014–1021.
15 W. van der Stam, J. J. Geuchies, T. Altantzis, K. H. van den Bos, J. D. Meeldijk, S. Van Aert, S. Bals, D. Vanmaekelbergh and C. de Mello Donega, *J. Am. Chem. Soc.*, 2017, **139**, 4087–4097.
16 D. B. Straus and R. J. Cava, *ACS Appl. Mater. Interfaces*, 2022, **14**, 34884–34890.
17 T. Qiao, D. Parobek, Y. Dong, E. Ha and D. H. Son, *Nanoscale*, 2019, **11**, 5247–5253.
18 D. Chen, G. Fang, X. Chen, L. Lei, J. Zhong, Q. Mao, S. Zhou and J. Li, *J. Mater. Chem. C*, 2018, **6**, 8990–8998.

Published on 27 July 2024. Downloaded by Xian Jiaotong University on 10/11/2024 2:45:41 AM.

19 J. Shi, M. Wang, C. Zhang, J. Wang, Y. Zhou, Y. Xu and N. V. Gaponenko, *Mater. Today Chem.*, 2023, **29**, 101480.
20 C. Y. Zhong, L. Li, Q. Chen, K. Z. Jiang, F. T. Li, Z. Q. Liu and Y. Chen, *Adv. Opt. Mater.*, 2022, **11**, 2202321.
21 C. Zhang, Z. Wang, M. Wang, J. Shi, J. Wang, Z. Da, Y. Zhou, Y. Xu, N. V. Gaponenko and A. S. Bhatti, *ACS Appl. Mater. Interfaces*, 2023, **15**, 35216–35226.
22 D. Rossi, D. Parobek, Y. Dong and D. H. Son, *J. Phys. Chem. C*, 2017, **121**, 17143–17149.
23 Z. J. Li, E. Hofman, J. Li, A. H. Davis, C. H. Tung, L. Z. Wu and W. Zheng, *Adv. Funct. Mater.*, 2017, **28**, 1704288.
24 X. Zhang, B. Xu, J. Zhang, Y. Gao, Y. Zheng, K. Wang and X. W. Sun, *Adv. Funct. Mater.*, 2016, **26**, 4595–4600.
25 C. Zhang, M. Wang, J. Shi, J. Wang, Z. Da, Y. Zhou, Y. Xu, N. V. Gaponenko and A. S. Bhatti, *Front. Chem.*, 2023, **11**, 1199863.
26 M. Fan, J. Huang, L. Turyanska, Z. Bian, L. Wang, C. Xu, N. Liu, H. Li, X. Zhang, C. Zhang and X. Yang, *Adv. Funct. Mater.*, 2023, 2215032, DOI: **10.1002/adfm.202215032**.
27 D. Chen, S. Zhou, G. Fang, X. Chen and J. Zhong, *ACS Appl. Mater. Interfaces*, 2018, **10**, 39872–39878.
28 J. Guo, M. Lu, X. Zhang, S. Sun, C. Han, Y. Zhang, X. Yang, S. V. Kershaw, W. Zheng and A. L. Rogach, *ACS Nano*, 2023, **17**, 9290–9301.
29 L. Ding, B. Borjigin, Y. Li, X. Yang, X. Wang and H. Li, *ACS Appl. Mater. Interfaces*, 2021, **13**, 51161–51173.
30 I. Rosa-Pardo, A. Ciccone, R. Arenal, R. E. Galian and J. Pérez-Prieto, *Chem. Mater.*, 2023, **35**, 7011–7019.
31 R. S. Ningthoujam, V. Sudarsan, R. K. Vatsa, R. M. Kadam, Jagannath and A. Gupta, *J. Alloys Compd.*, 2009, **486**, 864–870.
32 Y. Li, C. Wang, G. Hu, W. Meng, S. Sui and Z. Deng, *Chem. Commun.*, 2022, **58**, 941–944.
33 A. K. Guria, S. K. Dutta, S. D. Adhikari and N. Pradhan, *ACS Energy Lett.*, 2017, **2**, 1014–1021.
34 Q. Zhong, M. Cao, H. Hu, D. Yang, M. Chen, P. Li, L. Wu and Q. Zhang, *ACS Nano*, 2018, **12**, 8579–8587.
35 D. Parobek, B. J. Roman, Y. Dong, H. Jin, E. Lee, M. Sheldon and D. H. Son, *Nano Lett.*, 2016, **16**, 7376–7380.
36 J. Zhu, X. Yang, Y. Zhu, Y. Wang, J. Cai, J. Shen, L. Sun and C. Li, *J. Phys. Chem. Lett.*, 2017, **8**, 4167–4171.
37 D. Yan, S. Zhao, H. Wang and Z. Zang, *Photonics Res.*, 2020, **8**, 1086.
38 J. Ren, X. Zhou and Y. Wang, *Nano Res.*, 2020, **13**, 3387–3395.
39 J. Ma, Q. Yao, J. A. McLeod, L. Y. Chang, C. W. Pao, J. Chen, T. K. Sham and L. Liu, *Nanoscale*, 2019, **11**, 6182–6191.
40 W. J. Mir, Y. Mahor, A. Lohar, M. Jagadeeswararao, S. Das, S. Mahamuni and A. Nag, *Chem. Mater.*, 2018, **30**, 8170–8178.
41 K. Du, L. He, S. Song, J. Feng, Y. Li, M. Zhang, H. Li, C. Li and H. Zhang, *Adv. Funct. Mater.*, 2021, **31**, 2103275.
42 G. Jiang, C. Guhrenz, A. Kirch, L. Sonntag, C. Bauer, X. Fan, J. Wang, S. Reineke, N. Gaponik and A. Eychmuller, *ACS Nano*, 2019, **13**, 10386–10396.
43 Y. Yu, Y. Liang, J. Yong, T. Li, M. S. Hossain, Y. Liu, Y. Hu, K. Ganesan and E. Skafidas, *Adv. Funct. Mater.*, 2021, **32**, 2106387.

 This journal is © The Royal Society of Chemistry 2024